Author/s:
Robinson, DL;Jiang, H;Song, Q;Yates, C;Lee, PVS;Wark, JD

Title:
The application of finite element modelling based on clinical pQCT for classification of fracture status

Date:
2019-02-15

Citation:
Robinson, D. L., Jiang, H., Song, Q., Yates, C., Lee, P. V. S. & Wark, J. D. (2019). The application of finite element modelling based on clinical pQCT for classification of fracture status. Biomechanics and Modeling in Mechanobiology, 18 (1), pp.245-260. https://doi.org/10.1007/s10237-018-1079-7.

Persistent Link:
https://hdl.handle.net/11343/249521

THE APPLICATION OF FINITE ELEMENT MODELLING BASED ON CLINICAL PQCT FOR CLASSIFICATION OF FRACTURE STATUS

Dale L. Robinson[a] , Hongyuan Jiang[b], Qichun Song[b,c], Christopher Yates[d], Peter Vee Sin Lee[a], John D. Wark[b,e]

[a]Department of Biomedical Engineering, University of Melbourne, Melbourne, Victoria, Australia

[b]University of Melbourne Department of Medicine, Royal Melbourne Hospital, Melbourne, Victoria, Australia

[c]Department of Orthopaedics, 2nd affiliated Hospital, Xi'an Jiaotong University

[d]Department of Diabetes and Endocrinology, Royal Melbourne Hospital, Melbourne, Victoria, Australia

[e]Bone and Mineral Medicine, Royal Melbourne Hospital, Melbourne, Victoria, Australia

Submitted as an original article to the Biomechanics and Modeling in Mechanobiology

Word count: Text: 4,975 (Introduction to Discussion), Abstract: 316.

12 April 2018

Corresponding author:

Peter Vee Sin Lee

Department of Biomedical Engineering

University of Melbourne, Victoria 3010, Australia

Email: pvlee@unimelb.edu.au

23 Phone: +61 3 8344 4426

24 Fax: +61 3 8344 4290

Abstract:

Fracture risk assessment using dual-energy X-ray absorptiometry (DXA) frequently fails to diagnose osteoporosis amongst individuals who later experience fragility fractures. Hence more reliable techniques that improve the prediction of fracture risk are needed. In this study, we evaluated a finite element (FE) modelling framework based on clinical peripheral quantitative computed tomography (pQCT) imaging of the tibial epiphysis and diaphysis to predict the stiffness at these locations in compression, shear, torsion and bending. The ability of these properties to identify a group of women who had recently sustained a low-trauma fracture from an age- and weight-matched control group was determined and compared to clinical pQCT and DXA properties and structural properties based on composite beam theory. The predicted stiffnesses derived from the FE models and composite beam theory were significantly different ($p<0.05$) between the control and fracture groups, whereas no meaningful differences were observed using DXA and for the stress-strain indices (SSIs) derived using pQCT. The diagnostic performance of each property was assessed by the odds ratio (OR) and the area under the receiver operating curve (AUC), and were each greatest for the FE-predicted shear stiffness (OR=16.09, 95% CI: 2.52-102.56, p=0.003) (AUC: 0.80, 95% CI: 0.67-0.93). The clinical pQCT variable total density (ρ_{tot}) and a number of structural and FE-predicted variables had a similar probability of correct classification between the control and fracture groups (i.e., ORs and AUCs with mean values greater than 5.00 and 0.80, respectively). In general, the diagnostic characteristics were lower for variables derived using DXA and for the SSIs (i.e., ORs and AUCs with mean values of 1.65-2.98 and 0.64-0.71, respectively). For all properties considered, the trabecular-dominant tibial epiphysis exhibited enhanced classification characteristics, as compared to the cortical-dominant tibial diaphysis. The results of this study demonstrate that bone properties may be derived using FE

48 modelling that have the potential to enhance fracture risk assessment using conventional pQCT or
49 DXA instruments in clinical settings.
50

1 Introduction

Osteoporotic fractures are a global health concern among the elderly and have been linked to increased hospitalisation, morbidity and mortality [1–3]. Areal bone mineral density (aBMD) measured by dual-energy X-ray absorptiometry (DXA) is currently the clinical 'gold standard' for osteoporosis diagnosis and low BMD has been widely recognised as a risk factor for fracture [4,5]. However, a large proportion of individuals who are not diagnosed as osteoporotic by DXA still experience low trauma bone fracture [6,7]; hence, there remains a need to develop new clinical methods that better identify individuals at risk of fracture.

The strength of bone changes with "bone quality" and is a function of its structural architecture and constituents [8,9]. Quantitative computed tomography (QCT) provides measurements of volumetric BMD (vBMD), which is dependent on bone structure and composition. The vBMD derived at each voxel in a QCT scan may be converted into an equivalent Young's modulus (E), and using composite beam theory, the axial, bending and torsional rigidities of the bone may be calculated [10,11]. These structural properties have been shown to provide superior fracture risk predictions compared with clinical radiographic criteria [12,13]. Bone strength metrics such as stress-strain indices for bending (SSI_x and SSI_y) and torsion (SSI_{pol}) have also been used for fracture risk prediction [14–16]. These indices compare the structural rigidity of cortical bone to an identically-shaped bone with physiologically normal cortical density (1200 mg/cm^3), and have been shown to predict 40-80% of variance in the bone failure loads for 3-point bending [17,18] and compression [17–20]. A limitation of the aforementioned structural properties and strength indices is that they neglect three-dimensional (3D) effects, such as transverse shear and volume changes (Poisson effect). Techniques that consider 3D bone loading may offer some improvement in predictions of bone fracture risk, as compared with current methods.

Finite element (FE) models of cadaveric bones created from non-invasive imaging, such as peripheral QCT (pQCT), have demonstrated an excellent ability to predict bone fracture strength for bending and compression, accounting for 70-90% of variance between specimens [21–23]. Further, FE models derived from HR-pQCT [24,25] or QCT [26] have demonstrated good classification characteristics for identifying fracture status with area under the receiver operating curve (AUC) of 0.69-0.85. However, assessing fracture risk by QCT or HR-pQCT in a clinical setting poses three dilemmas: (1) the long time required to setup and analyse patient-specific FE models (3.5-10 hours [27]), (2) the large radiation dose associated with QCT, which for a 10 cm 3D scan of L1 and L2 or a 15 cm 3D scan of the proximal femur ranges from 1.5 to 3.0 mSv [28] and, (3) the prohibitively high costs involved with either purchasing or scanning with a HR-pQCT system. A novel approach is needed to address these challenges facing the application of FE modelling as an effective tool for clinical assessment of bone properties and fracture risk. In the study described here we have investigated whether FE modelling derived from tibial pQCT images may provide a solution.

Clinical tibia pQCT imaging typically targets two locations, the trabecular-dominant distal epiphysis (4% site of the tibial length from the distal end) and the cortical-dominant diaphysis (for example, the 66% site) [15,29]. To limit radiation dose and scan time, only a single cross-section ~2 mm thick is obtained at these two locations. By generating an FE model based upon these cross-sections, all of the aforementioned issues would be addressed: the radiation dose and scan time would be minimal and within clinical imaging protocols, and the FE model simplicity would allow its construction to be quick and easily automated. While this FE model would not represent the entire length of bone, it would account for three-dimensional stresses that are neglected when using structural properties or strength indices.

97 The aims of the current study were to (1) develop an FE model based on clinical pQCT
98 imaging protocols that predicted the compressive, shear, torsional and bending stiffness of tibial
99 epiphysis and diaphysis, and (2) to compute and compare the diagnostic characteristics of DXA,
100 pQCT, structural and FE model variables to identify individuals who have recently sustained a
101 low-trauma fracture.

102 # 2 Materials and Methods

103 ## 2.1 Study design

104 This study assessed the ability of FE-predicted stiffness variables derived from pQCT scans of the
105 tibia to distinguish between patients who had recently sustained a low-trauma fracture at another
106 skeletal site (fracture group) and subjects who had no prior fragility fracture history (control
107 group). The properties of the intact tibia were assumed representative of the subject's current
108 skeletal health, which was assumed deficient for the fracture patients. The tibia was considered
109 because it is readily accessed by a pQCT scanner, it is a site that has been well-documented to
110 exhibit changes in its micro-architecture due to aging and osteoporosis (see review by [30]), and
111 because tibial parameters have been associated with osteoporotic fractures at any skeletal site [31].
112 The classification analysis was repeated for structural properties calculated from composite beam
113 theory, for routine properties used in clinical pQCT imaging and for DXA-derived measurements
114 of aBMD for the total hip and lumbar spine.
115

116 ## 2.2 Participants

117 The fracture group comprised 23 post-menopausal women [age 64.4±8.3 years (mean±SD)] who
118 had experienced a low-trauma fracture (i.e., a fracture incurred from trauma equivalent to or less

than a fall from standing height). Each patient of the fracture group had at least one tibia without fracture and these patients were scanned within three months post-fracture using pQCT and DXA (see scanning protocol below). The control group comprised 23 post-menopausal women (age 64.8±6.8 years) that had no prior history of fracture to the imaged tibia and who had not incurred any previous fragility fractures. Healthy controls were recruited through electronic and paper-based advertisements at the University of Melbourne and the Royal Melbourne hospital. The control participants were included if they were greater than 50 years of age, had no prior history of medical conditions that may affect bone health (e.g., osteoporosis, hyperthyroidism, diabetes), and if using hormone replacement therapy were receiving a stable dose. Control and fracture group patients were also selected to achieve a height- and weight-match between the groups. All low-trauma fracture patients were recruited through the Royal Melbourne Hospital Fracture Capture program [32]. Ethics approval for this study was obtained from the Melbourne Health Human Research Ethics Committee [ID MH2014.143]. Patients provided written informed consent before participation.

2.3 pQCT and DXA scanning protocol

A Stratec XCT-3000 pQCT scanner (Medizintechnik, Pforzheim, Germany) running operating software version 6.20 acquired axial cross-sections of the tibia. Scans were performed by an experienced technologist according to the XCT-3000 software user's manual. Axial images were obtained at two sites, 4% and 66% of the bone length measured proximally from the distal articular surface (Fig. 1A). A scout scan was used to locate the distal articular surface of the tibia. Each cross-section had a slice thickness of 2 mm and a 0.4 mm voxel size. Tibia length (L_{tibia}) was measured manually as the vertical distance from the medial malleolus to the inferior apex of the patella whilst the knee was flexed at 90 degrees. Daily phantom scans were performed to assess

long-term scanner stability and, to date, no alterations of the calibration function have been required.

A fan-beam densitometer (Horizon QDR 4500A, Hologic Inc., Bedford, MA, USA) was used to scan the hip and lumbar spine of each subject. The scans were analysed using the manufacturer's commercial software (version 9.10D) to obtain aBMD measurements for the femoral neck, lumbar spine and total hip. All scans were performed in array mode by an experienced operator and the 12-month precision of the scanner for the spine phantom was 0.39% for aBMD and 0.58% for bone mineral content [33].

2.4 pQCT properties

The tibial bone pQCT images were manually segmented using commercially-available software (Matlab; version R2016b Mathworks, Natick, MA, USA), and the Hounsfield unit (H_f) of each voxel was converted to apparent bone mineral density (ρ_{app}) using Eq. 1 (see also Fig. 1B), which was derived for the scanner based on the specifications provided in the open-source software BoneJ [34]. These segmented data were used to derive standard pQCT variables including: total area (a_{tot}) and total density (ρ_{tot}). The bone stress-strain indices for bending (SSI_x and SSI_y) and torsion (SSI_{pol}) were calculated for each of the 4% and 66% locations (Eqs. 2-3).

$$\rho_{app} = 1.484H_f - 48965\ , \tag{1}$$

$$SSI_x = \sum \frac{CD_i A_i {d_{y,i}}^2}{CD_{norm} d_{ymax}},\ SSI_y = \sum \frac{CD_i A_i {d_{x,i}}^2}{CD_{norm} d_{xmax}}, \tag{2}$$

$$SSI_{pol} = \sum \frac{CD_i A_i {r_i}^2}{CD_{norm} r_{max}}\ , \tag{3}$$

where ρ_{app} is the apparent bone mineral density; H_f is the Hounsfield unit; CD_i is the cortical bone density; A_i, is the area of voxel i; $d_{x,i}$, $d_{y,i}$, r_i are the horizontal, vertical and radial distances of voxel i from the cortex centroid respectively; CD_{norm} is the normal

physiological density of cortical bone (1200 g/cm^3); and d_{xmax}, d_{ymax} and r_{max} are the maximum x, y and radial distances of a cortical bone voxel from the cortex centroid, respectively. The x- and y-axes were aligned with the minimum and maximum neutral axes, respectively, derived from the cortical bone in each cross-section.

2.5 Structural properties

The Young's modulus (E_i) of cortical and trabecular bone was calculated at each voxel i in the segmented pQCT images using Eq. 4, which was derived from mechanical tests performed on small cylindrical bone specimens extracted from the tibia [11] (see also Fig. 1C). Axial and torsional rigidities (EA, GJ, respectively) and the bending rigidity about the x and y-axes (EI_x and EI_y, respectively) were calculated for each cross-section using Eqs. 5-8.

$$E_i = 15520\rho_{app,i}^{1.93} \quad (4)$$

$$EA = \sum E_i a_i \quad (5)$$

$$\mathrm{GJ} = \sum G_i(x_i^2 + y_i^2)a_i \quad (6)$$

$$\mathrm{EI}_x = \sum E_i y_i^2 a_i \,;\, \mathrm{EI}_y = \sum E_i x_i^2 a_i \quad (7)$$

$$\bar{x} = \frac{\sum E_i x_i a_i}{\sum a_i};\ \bar{y} = \frac{\sum E_i y_i a_i}{\sum a_i}, \quad (8)$$

where E_i, G_i, $\rho_{app,i}$ and a_i are, respectively, the Young's modulus, shear modulus, apparent density and area of voxel i. For transverse cross-sections, G_i was taken as $E_i/2.6$ [12]. *EA = axial rigidity, GJ = torsional rigidity, EI_x and EI_y are the bending rigidities about the x- and y-axes. The x- and y-axes were aligned to the minimum and maximum neutral axes, respectively, derived using both the cortical and trabecular bone in each cross-section. $\bar{x}$, $\bar{y}$ are the coordinates of the density-weighted centroid for the cross-section, and x_i, y_i represent the horizontal and vertical distance between voxel i and the density-weighted centroid.*

2.6 FE model properties

Using Matlab, the segmented pQCT images were extruded by the 2 mm slice thickness to generate a mesh of 0.4x0.4x2 mm elements (Fig. 2A). Each element was modelled as a linear-elastic material with the respective E_i and G_i set to the values calculated above (see Section 2.5) and the mesh was re-sliced in the axial direction into 0.4 mm cubic elements (Fig. 2B). Each voxel mesh was used to create a FE model in the commercial software Abaqus (version 6.11, Simulia, Dassault Systemes, Providence, RI, USA). Although the cubic element size of 0.4 mm was too large to capture the topology of individual trabeculae, which for the distal tibia vary between 0.10 to 0.15 mm [35,36], previous FE models of the femur that represented cortical and trabecular bone with a continuum of elements that incorporated edge lengths greater than 1.5 mm were found to predict experimental bending and compressive strengths, with coefficients of determination (R^2) between 0.85 and 0.90 [37–39]. Hence, the continuum mesh with an element size of 0.4 mm implemented in the current study was assumed sufficient for modelling the contribution of the trabecular and cortical bone to the total stiffness of the 2 mm thick tibial cross-sections.

The origin of the models was set as the density-weighted centroid (Eq. 9), the x- and y-axes were aligned with the minimum and maximum neutral axes, respectively, and the z-axis was normal to the cross-section. Four load cases were considered for all FE models; axial compression, shear, torsion and bending (Figs. 3A-D). Axial compression was simulated by a 0.01 mm displacement of the superior surface towards the inferior surface. Shear was simulated by a 0.01 mm displacement of the superior surface in the direction of either the x- or y-axes. Torsion was simulated by a 0.0001 radian rotation of the inferior surface about the z-axis. Bending was simulated by a 0.0001 radian rotation of the inferior surface about either the x- and y-axes (i.e., cross-section neutral axes). These idealised loading conditions would almost certainly differ from

tibial loading in vivo, where compression, shear, torsion and bending occur simultaneously [40]. Logically, however, a bone that more weakly resists an idealised load has a greater risk of fracturing for the combined load case. Indeed, this assumption has been adopted in previous micro-finite element studies, where the strength of the tibia or radius was calculated for idealised axial compression, and used to assess fracture risk [31].

The reaction forces and moments predicted from the simulations were divided by the respective applied displacement or rotation to determine the compressive stiffness (k_{comp}), shear stiffness (k_{shear}), torsional stiffness ($k_{torsion}$) and bending stiffness (k_{bend}) of each cross-section. Although strain-based failure criteria in FE models have been previously used to predict bone strength [21], this was not possible here because results from a mesh convergence study showed the absolute strain predictions from our FE models were unreliable for 0.4 mm cubic elements implemented in a 2 mm thick cross-section (data not shown). In all simulations, the unprescribed degrees-of-freedom of the inferior and superior surfaces were set to zero to account for the resistance of the surrounding bone.

2.7 FE model verification

To verify that the FE model predictions were independent of the FE mesh size, a mesh convergence analysis was performed. For the 4% and 66% sites of a representative fracture subject, the original 0.4 mm cubic elements of the FE model were resized to 0.1, 0.2 or 1.0 mm (Fig. 4). The apparent density and, hence, modulus of the elements for each different mesh size was calculated at their respective centroids in Matlab using a piecewise cubic surface fitted to the density distribution of the original pQCT image. The FE model for each mesh was used to simulate the four load cases, from which the corresponding FE model properties were calculated.

The rigid boundary conditions together with the thin cross-sections would generate some stress concentrations in the FE model. However, by applying identical boundary conditions for all FE models, it was assumed that the relative differences in stiffness predicted between the control and fracture group would be consistent regardless of the cross-section thickness. To support this reasoning, three FE models of 50 mm diameter cylindrical tubes of Young's modulus 0.15 GPa, 0.16 GPa and 0.17 GPa were created that were either 2 mm or 100 mm thick (see Supplementary material Fig. 1) and used to simulate the aforementioned compression, shear, torsion and bending load cases. The relative changes in stiffness predicted as the Young's modulus was varied were identical for each tube thickness (see Supplementary material Table 1), thus, confirming that relative differences in FE-predicted bone properties were unlikely to have been affected by cross-section thickness.

2.8 Statistical Analysis

Significant differences between the control and fracture groups were assessed by a two-sample Kolmogorov-Smirnov test ($p<0.05$) which makes no assumption about the distribution of the data. To identify collinearity, variance inflation factors (VIFs) were derived from multivariate linear regressions where the predictors were based on either the pQCT properties (a_{tot}, ρ_{tot}, SSI_x, SSI_y and SSI_{pol}), DXA properties (aBMD lumbar, aBMD femoral neck, aBMD total hip), structural properties (EA, GJ, EI_x and EI_y) or FE model properties (k_{comp}, k_{shear}, $k_{torsion}$ and k_{bend}), and any unrelated property taken as the dependent variable. Age, height and weight were also included in each regression and collinearity was assumed for a VIF greater than 5.0 [41].

To evaluate the relationship between fracture status and explanatory variables, a binary logistical regression was performed. The fracture status was considered a categorical variable and each predictor, the pQCT, DXA, structural and FE model properties was considered in independent

regressions, with each being adjusted for confounding variables, such as age, height and weight. Regression results were summarised by the odds ratio (OR) per standard deviation decrease in the predictor. For sets of properties found to be collinear, the property with the greatest average OR was included in the classification analysis, while the remaining collinear variables were excluded.

The ability of the predictors to classify patients as controls or fracture patients was evaluated by constructing receiver operating characteristic (ROC) curves based on each logistical regression. The sensitivity (ability to correctly identify fracture group patients) and specificity (ability to correctly identify control group patients) was determined for each predictor using standard diagnostic formulae [42], with optimal values selected based on the Youden's J statistic, which represents the maximum correct classification rate [43]. The area under the receiver operating curve (AUC) was also calculated for all predictors. All statistical analyses were performed using SPSS (version 24; SPSS Inc., Chicago, IL, USA).

3 Results

Descriptive characteristics of the control and fracture groups are provided in Table 1, where no significant differences were noted between the groups. The FE model verification analysis indicated that for a cubic element size of 1 mm applied to the 4% and 66% sites, the FE model properties (k_{comp}, k_{shear}, $k_{torsion}$ and k_{bend}) varied considerably from their corresponding values computed with a cubic element size of 0.1 mm by -2.4 to 96.7% (Table 2). However, for smaller cubic element sizes of 0.4 and 0.2 mm, the FE model properties differed from those calculated with a cubic element size of 0.1 mm by -1.4 to -0.2%. These changes were considered minimal and verified that the FE model properties were independent of mesh size for cubic elements less than or equal to 0.4 mm.

The maximum and minimum principal stresses for each load case predicted by the FE models of a representative participant of the control group are provided for the 4% and 66% sites in Fig. 5. At the 4% site, the maximal principal stresses were confined to the thin layer of cortical bone for all load cases. In comparison, at the 66% site the maximal principal strains were located closer to the periosteum for torsion and bending, at both the endosteum for shear, and across the entire cortex for compression. The only exception to these trends was the maximum principal stress, which was largest for the trabecular bone at the 4% site and for the very low stiffness element of the medullary cavity for the 66% site. The reaction force or moment for each load case was used to calculate the compression, shear, torsion and bending stiffness for each site (Table 3).

At the 4% site, all structural and FE model properties differed significantly ($p<0.05$) between the control and fracture groups (Table 4). Considering the pQCT variables, only ρ_{tot} differed significantly between the two groups at the 4% site ($p=0.002$). No variables were observed to differ significantly between the controls and fracture group at the 66% site. There was no significant difference observed between the two groups for the aBMDs derived using DXA. Box and whisker plots of key variables of each imaging modality (i.e., DXA, pQCT, structural and FE model properties) are provided in Fig. 6, which illustrates the distribution of variables between the controls and fracture group.

Based upon the linear multivariate regressions for the DXA, pQCT, structural and FE model properties, the VIFs for age, height and weight were less than 5.0 for all groups and sites (Table 5), indicating there was no collinearity between these variables and the bone properties presented in the current study. For the DXA variables of the control group, aBMD for the femoral neck and total hip each had a VIF greater than 5.0, implying collinearity between these variables. aBMD for the total hip was subsequently included in the classification analysis since it had the

greatest average OR (2.98, 95% CI: 1.24-7.13; Table 6). At the 4% site of both the control and fracture group, collinearity was observed between all properties within each of the pQCT, structural or FE model modalities (Table 5). Since ρ_{tot}, EA and k_{shear} had the greatest OR for each modality, these were the only variables included in the correlation analysis for the pQCT, structural and FE model properties (Table 6). Similarly, for the pQCT and FE model properties at the 66% site, the respective variables were each found to be collinear, with the SSI_x and $k_{torsion}$ properties included in the classification analysis based upon their greater ORs. However, for the structural properties at the 66% site, only EI_y and GJ were found to be collinear (Table 5). Since GJ had a greater average OR compared to EI_y, it was included in the classification analysis along with the independent variables EA and EI_x.

Considering properties derived at the 4% site and adjusting for age, weight and height, the fracture odds increased most with a decrease in k_{shear} (OR=16.09, 95% CI: 2.52-102.56, p=0.003) (Table 6). For variables included in the classification analysis, odds ratios that were significant ($p<0.05$) with a mean value greater than 5.0 were also observed for the structural property EI_y and the pQCT property ρ_{tot}. At the 66% site, the odds of fracture were not significantly related to any of pQCT, structural or FE model properties included in the classification analysis. In the case of DXA, the odds ratio was significant for aBMD of the total hip (OR=2.98, 95% CI: 1.24-7.13, p=0.01).

The greatest AUC was observed at the 4% site for the FE model property k_{shear} (AUC: 0.81, 95% CI: 0.69-0.94). Youden's J statistic was greatest for this variable, indicating the optimal combination of sensitivity and specificity (78.3% and 82.6%, respectively). AUCs of a similar magnitude were observed at the 4% site for the structural property EI_y (AUC: 0.80, 95% CI: 0.67-0.93) and the pQCT property ρ_{tot} (AUC: 0.80, 95% CI: 0.67-0.93). The greatest AUC observed for

the DXA properties was aBMD for the total hip (AUC: 0.71, 95% CI: 0.56-0.86). The AUCs observed at the 66% site provided a poor classification between the controls and fracture group, with mean values between 0.61 and 0.65.

4 Discussion

In this study an FE model based on pQCT was proposed and its diagnostic ability to identify patients who had recently sustained a low trauma fracture was compared with structural properties and clinical pQCT and DXA properties. For this analysis, pQCT scans of the tibial epiphysis and diaphysis were obtained for two groups of post-menopausal women; a group who had recently sustained a low-trauma fracture at another skeletal site (fracture group) and an age-matched group with no history of tibial fracture and at the time of this study were considered to be at low risk of incurring a low-trauma fracture (control group). The properties of the intact tibia were assumed to be representative of each subject's current skeletal health, which was hypothesised to be deficient in the fracture group.

Whilst FE models based on individual bone cross-sections from pQCT imaging have been previously developed [44], to our knowledge, this is the first study to (1) use these techniques to assess fracture status *in vivo* and, (2) compare its diagnostic performance with existing fracture risk assessment methods. The FE model property k_{shear} had the greatest OR (16.09; 95% CI: 2.52-102.56) and AUC (0.81; 95% CI: 0.69-0.94), indicating this variable had the greatest probability to correctly differentiate the fracture group from the control group. The diagnostic characteristics were marginally lower for the structural property EA (OR: 10.51; 95% CI: 2.07-53.44) (AUC: 0.80; 95% CI: 0.67-0.93) and the pQCT property ρ_{tot} (OR: 12.86; 95% CI: 2.51-65.76) (AUC: 0.80; 95% CI: 0.67-0.93). For DXA, aBMD obtained for the total hip had a lower, yet still

346 significant, diagnostic performance (OR: 2.98; 95% CI: 1.24-7.13) (AUC: 0.71, 95% CI: 0.56-
347 0.86). The stress-strain indices used in clinical pQCT imaging had significantly reduced
348 performance compared to the aforementioned variables, with ORs less than 2.02 and an AUC of
349 0.65, 95% CI: 0.49-0.81. The trabecular-dominant distal tibial epiphysis yielded enhanced
350 predictions of fracture status compared to the diaphysis. This suggests that trabecular bone
351 properties are more sensitive than cortical bone properties for identifying fracture risk, a finding
352 supported by others [45,46].

353 These findings suggest that simple pQCT measurements (ρ_{tot}) and predictions of bone
354 stiffness obtained using FE modelling may be used to add to the diagnostic accuracy of DXA.
355 Whilst this finding is consistent with others who compared pQCT, HR-pQCT and/or QCT to DXA
356 in fragility and radial fracture assessment [25,47–49], it is acknowledged that DXA is not typically
357 recommended for early postmenopausal women aged less than 60 years, unless they possess a
358 clinical risk factor [50,51]. Although the low-trauma fractures sustained by the fracture group
359 patients is a well-established risk factor that improves the sensitivity of fracture prediction using
360 DXA [52], this was not the case for the control subjects, who did not present with any apparent
361 fracture risks. Hence, a reduced fracture risk sensitivity would be expected for the controls using
362 DXA, which would explain its reduced diagnostic accuracy compared to the other modalities
363 considered in the current study.

364 The classification performance obtained for the structural and FE-derived properties also
365 support previous findings that other bone properties exist that better correlate with fracture
366 properties compared with stress-strain indices [18]. In this study, the differences between the
367 groups appeared best characterised by differences in the trabecular bone, which may explain the
368 poor diagnostic performance of the stress-strain indices, since they are calculated based solely on

the density and distribution of cortical bone. This effect may have also reduced the diagnostic performance of the DXA-derived aBMD measurements, since the imaging sites have proportionally greater amounts of cortical bone compared to the tibial epiphysis.

This study had limitations that are acknowledged. The generalization of the findings in this study may be limited by the low number of subjects in the control and fracture group. The number of participants was motivated by the intentions of this work, specifically to present the FE modelling framework and to examine whether the classification characteristics of this model appeared to classify fracture risk favourably, albeit for a relative small sample of subjects. In future work, we intend to re-evaluate the classification characteristics of all presented bone properties across a much larger cohort.

The distribution of fracture sites across the fracture group patients was inhomogeneous, with a number of different upper or lower limb fractures observed. These fracture sites were a consequence of the recruitment of low-trauma fracture patients from a fracture liaison service, a cohort which predominately comprise peripheral fractures, as compared to the prevalence of hip and vertebral fractures typically encountered for osteoporotic fracture groups [53–55]. However, given that pQCT specifically images the peripheral skeleton, it would be suggested that the prediction of fracture risk based on FE-derived bone properties is ideal for predicting fracture risk in cohorts with increased limb fracture prevalence, as considered in the current study. When further considering the different fracture sites, it is feasible that the seven patients who sustained a low-trauma lower limb fracture may have experienced bone remodelling of their intact tibia due to the loss in mobility and change in loading experienced following the injury. Compared to the bone remodelling cycle of 120-200 days [56], it is feasible that some remodelling may have taken place from post-fracture to pQCT imaging, which for these patients was on average 64.4 days (range:

30-88 days). However, there was no significant differences observed between fracture group patients with and without a lower limb fracture (Supplementary material Table 2), which would support the reasoning that any changes in bone structure due to different post-fracture tibial loadings between subjects were minor and considered unlikely to alter the findings of the current study.

Another evident issue is whether the fracture status of each subject was truly related to the structural properties at two discrete locations of the intact tibia. Whilst these sites are useful for comparing differences in cortical and trabecular bone structures at a consistent location, their ability to predict skeletal fracture risk relies on the assumption of uniform structural changes throughout the body. In reality, bone loss associated with aging or osteoporosis is not uniform across the body [57,58]. By acquiring pQCT scans at other locations such as the contralateral tibia or the forearms, the extent of the inhomogeneity may be evaluated, and possibly used to improve the diagnostic performance of the methods presented in the current study. We note, however, that previous longitudinal data has shown the tibia to be a reasonable predictor for all types of fragility fractures, including vertebrae, ribs or the appendicular skeleton [31].

A final limitation was that the loads applied in the FE model would differ from those encountered by tibiae *in vivo*. For example, the knee joint experiences both forces and bending moments that each change magnitude and direction during daily activities [59]. However, musculoskeletal loadings vary significantly between individuals [60–62] and obtaining these correct loading combinations for a large number of patients would not be feasible in a clinical setting. Therefore, idealising the loading conditions was the only practical option available, and adequately met the aims of our study since the classification analysis only considered differences in bone properties between the control and fracture groups.

In summary, we have demonstrated that FE models of individual pQCT cross-sections are likely to enhance diagnosis of fracture status compared to stress-strain indices used in pQCT image and aBMD measurements derived using DXA. Whilst it is feasible to apply these methods in prospective fracture risk diagnosis, caution should be exercised when generalising the findings of our study since it was cross-sectional in design and based on outcomes for a small number of relatively young subjects where DXA is known to be less sensitive for fracture risk assessment [50]. Hence, longitudinal data for a larger and, ideally, older cohort of patients are needed to confirm the outcomes based on our assessment of fracture status. Nevertheless, we would recommend caution when using pQCT properties such as SSIs for fracture risk prediction because our results suggest more accurate variables are available such as bone properties derived from FE modelling or structural analysis.

5 Acknowledgements

We thank all participants for consenting to provide their pQCT tibia scan data for this study. We duly acknowledge Ashwini Kale for diligently performing all pQCT scans, Richard Farrugia for facilitating patient recruitment and clinic coordination activities, and Associate Professor Andrew Bucknill for his strong support of the Royal Melbourne Hospital fracture liaison service. This work was supported by a collaborative PhD scholarship provided by the University of Melbourne and the China scholarship council to HJ.

References

[1] Nazrun, A. S., Tzar, M. N., Mokhtar, S. A., and Mohamed, I. N., 2014, "A Systematic Review of the Outcomes of Osteoporotic Fracture Patients after Hospital Discharge: Morbidity, Subsequent Fractures, and Mortality," Ther. Clin. Risk Manag., **10**, pp. 937–948.
[2] Sattui, S. E., and Saag, K. G., 2014, "Fracture Mortality: Associations with Epidemiology

and Osteoporosis Treatment," Nat. Rev. Endocrinol., **10**(10), pp. 592–602.
[3] Johnell, O., and Kanis, J. A., 2006, "An Estimate of the Worldwide Prevalence and Disability Associated with Osteoporotic Fractures," Osteoporos. Int., **17**(12), pp. 1726–1733.
[4] Stone, K. L., Seeley, D. G., Lui, L.-Y., Cauley, J. a, Ensrud, K., Browner, W. S., Nevitt, M. C., and Cummings, S. R., 2003, "BMD at Multiple Sites and Risk of Fracture of Multiple Types: Long-Term Results From the Study of Osteoporotic Fractures," J Bone Min. Res, **18**(11), pp. 1947–1954.
[5] Kanis, J. A., 2002, "Osteoporosis III: Diagnosis of Osteoporosis and Assessment of Fracture Risk," Lancet, **359**(9321), pp. 1929–1936.
[6] Schuit, S. C. ., van der Klift, M., Weel, A. E. A. ., de Laet, C. E. D. ., Burger, H., Seeman, E., Hofman, A., Uitterlinden, A. ., van Leeuwen, J. P. T. ., and Pols, H. A. ., 2004, "Fracture Incidence and Association with Bone Mineral Density in Elderly Men and Women: The Rotterdam Study," Bone, **34**(1), pp. 195–202.
[7] Siris, E. S., Miller, P. D., Barrett-Connor, E., Faulkner, K. G., Wehren, L. E., Abbott, T. A., Berger, M. L., Santora, A. C., and Sherwood, L. M., 2001, "Identification and Fracture Outcomes of Undiagnosed Low Bone Mineral Density in Postmenopausal Women: Results from the National Osteoporosis Risk Assessment.," JAMA, **286**(22), pp. 2815–2822.
[8] Seeman, E., and Delmas, P. D., 2006, "Bone Quality--the Material and Structural Basis of Bone Strength and Fragility.," N. Engl. J. Med., **354**(21), pp. 2250–2261.
[9] Ammann, P., and Rizzoli, R., 2003, "Bone Strength and Its Determinants," Osteoporos. Int., **14**(S3), pp. 13–18.
[10] Whealan, K. M., Kwak, S. D., Tedrow, J. R., Inoue, K., and Snyder, B. D., 2000, "Noninvasive Imaging Predicts Failure Load of the Spine with Simulated Osteolytic Defects.," J. Bone Joint Surg. Am., **82**(9), pp. 1240–1251.
[11] Morgan, E. F., Bayraktar, H. H., and Keaveny, T. M., 2003, "Trabecular Bone Modulus-Density Relationships Depend on Anatomic Site," J. Biomech., **36**(7), pp. 897–904.
[12] Snyder, B. D., Hauser-Kara, D. A., Hipp, J. A., Zurakowski, D., Hecht, A. C., and Gebhardt, M. C., 2006, "Predicting Fracture through Benign Skeletal Lesions with Quantitative Computed Tomography," J. BONE Jt. Surg., **88**–**A**(1), pp. 55–70.
[13] Snyder, B. D., Cordio, M. A., Nazarian, A., Kwak, S. D., Chang, D. J., Entezari, V., Zurakowski, D., and Parker, L. M., 2009, "Noninvasive Prediction of Fracture Risk in Patients with Metastatic Cancer to the Spine," Clin. Cancer Res., **15**(24), pp. 7676–7683.
[14] Erlandson, M. C., Kontulainen, S. A., Chilibeck, P. D., Arnold, C. M., Faulkner, R. A., and Baxter-Jones, A. D. G., 2012, "Former Premenarcheal Gymnasts Exhibit Site-Specific Skeletal Benefits in Adulthood after Long-Term Retirement," J. Bone Miner. Res., **27**(11), pp. 2298–2305.
[15] Duckham, R. L., Frank, A. W., Johnston, J. D., Olszynski, W. P., and Kontulainen, S. A., 2013, "Monitoring Time Interval for PQCT-Derived Bone Outcomes in Postmenopausal Women," Osteoporos. Int., **24**(6), pp. 1917–1922.
[16] Duckham, R. L., Baxter-Jones, A. D. G., Johnston, J. D., Vatanparast, H., Cooper, D., and Kontulainen, S., 2014, "Does Physical Activity in Adolescence Have Site-Specific and Sex-Specific Benefits on Young Adult Bone Size, Content, and Estimated Strength?," J. Bone Miner. Res., **29**(2), pp. 479–486.
[17] Lochmüller, E.-M., Lill, C. A., Kuhn, V., Schneider, E., and Eckstein, F., 2002, "Radius Bone Strength in Bending, Compression, and Falling and Its Correlation With Clinical

Densitometry at Multiple Sites," J. Bone Miner. Res., **17**(9), pp. 1629–1638.
[18] Kontulainen, S. A., Johnston, J. D., Liu, D., Leung, C., Oxland, T. R., and McKay, H. A., 2008, "Strength Indices from PQCT Imaging Predict up to 85% of Variance in Bone Failure Properties at Tibial Epiphysis and Diaphysis," J. Musculoskelet. Neuronal Interact., **8**(4), pp. 401–409.
[19] Ashe, M. C., Khan, K. M., Kontulainen, S. A., Guy, P., Liu, D., Beck, T. J., and McKay, H. A., 2006, "Accuracy of PQCT for Evaluating the Aged Human Radius: An Ashing, Histomorphometry and Failure Load Investigation," Osteoporos. Int., **17**(8), pp. 1241–1251.
[20] Muller, M. E., Webber, C. E., and Bouxsein, M. L., 2003, "Predicting the Failure Load of the Distal Radius," Osteoporos. Int., **14**(4), pp. 345–352.
[21] Pistoia, W., van Rietbergen, B., Lochmüller, E.-M., Lill, C. A., Eckstein, F., and Rüegsegger, P., 2002, "Estimation of Distal Radius Failure Load with Micro-Finite Element Analysis Models Based on Three-Dimensional Peripheral Quantitative Computed Tomography Images.," Bone, **30**(6), pp. 842–848.
[22] Varga, P., Baumbach, S., Pahr, D., and Zysset, P. K., 2009, "Validation of an Anatomy Specific Finite Element Model of Colles' Fracture," J. Biomech., **42**(11), pp. 1726–1731.
[23] Zysset, P. K., Dall'Ara, E., Varga, P., and Pahr, D. H., 2013, "Finite Element Analysis for Prediction of Bone Strength," Bonekey Rep., **2**(AUGUST), pp. 1–9.
[24] Nishiyama, K. K., Macdonald, H. M., Hanley, D. A., and Boyd, S. K., 2013, "Women with Previous Fragility Fractures Can Be Classified Based on Bone Microarchitecture and Finite Element Analysis Measured with HR-PQCT," Osteoporos. Int., **24**(5), pp. 1733–1740.
[25] Liu, X. S., Stein, E. M., Zhou, B., Zhang, C. A., Nickolas, T. L., Cohen, A., Thomas, V., McMahon, D. J., Cosman, F., Nieves, J., and others, 2012, "Individual Trabecula Segmentation (ITS)-Based Morphological Analyses and Microfinite Element Analysis of HR-PQCT Images Discriminate Postmenopausal Fragility Fractures Independent of DXA Measurements," J. Bone Miner. Res., **27**(2), pp. 263–272.
[26] Amin, S., Kopperdhal, D. L., Melton, L. J., Achenbach, S. J., Therneau, T. M., Riggs, B. L., Keaveny, T. M., and Khosla, S., 2011, "Association of Hip Strength Estimates by Finite-Element Analysis with Fractures in Women and Men," J. Bone Miner. Res., **26**(7), pp. 1593–1600.
[27] Kawalilak, C. E., Kontulainen, S. A., Amini, M. A., Lanovaz, J. L., Olszynski, W. P., and Johnston, J. D., 2016, "In Vivo Precision of Three HR-PQCT-Derived Finite Element Models of the Distal Radius and Tibia in Postmenopausal Women," BMC Musculoskelet. Disord., **17**(1), pp. 1–11.
[28] Engelke, K., Adams, J. E., Armbrecht, G., Augat, P., Bogado, C. E., Bouxsein, M. L., Felsenberg, D., Ito, M., Prevrhal, S., Hans, D. B., and Lewiecki, E. M., 2008, "Clinical Use of Quantitative Computed Tomography and Peripheral Quantitative Computed Tomography in the Management of Osteoporosis in Adults: The 2007 ISCD Official Positions," J. Clin. Densitom., **11**(1), pp. 123–162.
[29] Rinaldi, G., Wisniewski, C. A., Setty, N. G., and LeBoff, M. S., 2011, "Peripheral Quantitative Computed Tomography: Optimization of Reproducibility Measures of Bone Density, Geometry, and Strength at the Radius and Tibia," J. Clin. Densitom., **14**(3), pp. 367–373.
[30] Nishiyama, K. K., and Shane, E., 2013, "Clinical Imaging of Bone Microarchitecture with HR-PQCT," Curr. Osteoporos. Rep., **11**(2), pp. 147–155.
[31] Vilayphiou, N., Boutroy, S., Szulc, P., Van Rietbergen, B., Munoz, F., Delmas, P. D., and

Chapurlat, R., 2011, "Finite Element Analysis Performed on Radius and Tibia HR-PQCT Images and Fragility Fractures at All Sites in Men," J. Bone Miner. Res., **26**(5), pp. 965–973.

[32] Yates, C. J., Chauchard, M. A., Liew, D., Bucknill, A., and Wark, J. D., 2015, "Bridging the Osteoporosis Treatment Gap: Performance and Cost-Effectiveness of a Fracture Liaison Service," J. Clin. Densitom., **18**(2), pp. 150–156.

[33] Briggs, A. M., Perilli, E., Parkinson, I. H., Wrigley, T. V., Fazzalari, N. L., Kantor, S., and Wark, J. D., 2010, "Novel Assessment of Subregional Bone Mineral Density Using DXA and PQCT and Subregional Microarchitecture Using Micro-CT in Whole Human Vertebrae: Applications, Methods, and Correspondence Between Technologies," J. Clin. Densitom., **13**(2), pp. 161–174.

[34] Doube, M., Kłosowski, M., Arganda-Carreras, I., Cordelières, F. P., Dougherty, R. P., Jackson, J. S., Schmid, B., Hutchinson, J. R., and Shefelbine, S. J., 2010, "BoneJ: Free and Extensible Bone Image Analysis in ImageJ," Bone, **47**(6), pp. 1076–1079.

[35] Liu, X. S., Zhang, X. H., Sekhon, K. K., Adams, M. F., McMahon, D. J., Bilezikian, J. P., Shane, E., and Guo, X. E., 2010, "High-Resolution Peripheral Quantitative Computed Tomography Can Assess Microstructural and Mechanical Properties of Human Distal Tibial Bone," J. Bone Miner. Res., **25**(4), pp. 746–756.

[36] Thomsen, J. S., Laib, A., Koller, B., Prohaska, S., Mosekilde, L., and Gowin, W., 2005, "Stereological Measures of Trabecular Bone Structure: Comparison of 3D Micro Computed Tomography with 2D Histological Sections in Human Proximal Tibial Bone Biopsies," J.Microsc., **218**(0022–2720 (Print)), pp. 171–179.

[37] Keyak, J. H., Rossi, S. a, Jones, K. a, and Skinner, H. B., 1997, "Prediction of Femoral Fracture Load Using Automated Finite Element Modelling," J Biomech, **31**(2), pp. 125–133.

[38] Koivumäki, J. E. M., Thevenot, J., Pulkkinen, P., Kuhn, V., Link, T. M., Eckstein, F., and Jämsä, T., 2012, "Ct-Based Finite Element Models Can Be Used to Estimate Experimentally Measured Failure Loads in the Proximal Femur," Bone, **50**(4), pp. 824–829.

[39] Dragomir-Daescu, D., Op Den Buijs, J., McEligot, S., Dai, Y., Entwistle, R. C., Salas, C., Melton, L. J., Bennet, K. E., Khosla, S., and Amin, S., 2011, "Robust QCT/FEA Models of Proximal Femur Stiffness and Fracture Load during a Sideways Fall on the Hip," Ann. Biomed. Eng., **39**(2), pp. 742–755.

[40] Yang, P. F., Sanno, M., Ganse, B., Koy, T., Brüggemann, G. P., Müller, L. P., and Rittweger, J., 2014, "Torsion and Antero-Posterior Bending in the in Vivo Human Tibia Loading Regimes during Walking and Running," PLoS One, **9**(4).

[41] Ringle, C. M., Wende, S., and Becker, J.-M., 2015, "SmartPLS 3," Boenningstedt SmartPLS GmbH, http//www. smartpls. com.

[42] Lalkhen, A. G., and McCluskey, A., 2008, "Clinical Tests: Sensitivity and Specificity," Contin. Educ. Anaesthesia, Crit. Care Pain, **8**(6), pp. 221–223.

[43] Youden, W. J., 1950, "Index for Rating Diagnostic Tests," Cancer, **3**(1), pp. 32–35.

[44] Kourtis, L. C., Carter, D. R., Kesari, H., and Beaupre, G. S., 2008, "A New Software Tool (VA-BATTS) to Calculate Bending, Axial, Torsional and Transverse Shear Stresses within Bone Cross Sections Having Inhomogeneous Material Properties," Comput. Methods Biomech. Biomed. Engin., **11**(5), pp. 463–476.

[45] Melton, L. J., Christen, D., Riggs, B. L., Achenbach, S. J., Müller, R., Van Lenthe, G. H., Amin, S., Atkinson, E. J., and Khosla, S., 2010, "Assessing Forearm Fracture Risk in

Postmenopausal Women," Osteoporos. Int., **21**(7), pp. 1161–1169.
[46] Eser, P., Frotzler, A., Zehnder, Y., and Denoth, J., 2005, "Fracture Threshold in the Femur and Tibia of People with Spinal Cord Injury as Determined by Peripheral Quantitative Computed Tomography," Arch. Phys. Med. Rehabil., **86**(3), pp. 498–504.
[47] Boutroy, S., Van Rietbergen, B., Sornay-Rendu, E., Munoz, F., Bouxsein, M. L., and Delmas, P. D., 2008, "Finite Element Analysis Based on in Vivo HR-PQCT Images of the Distal Radius Is Associated with Wrist Fracture in Postmenopausal Women," J. Bone Miner. Res., **23**(3), pp. 392–399.
[48] Jamal, S. A., Gilbert, J., Gordon, C., and Bauer, D. C., 2006, "Cortical PQCT Measures Are Associated with Fractures in Dialysis Patients," J. Bone Miner. Res., **21**(4), pp. 543–548.
[49] Li, N., Li, X., Xu, L., Sun, W., Cheng, X., and Tian, W., 2013, "Comparison of QCT and DXA: Osteoporosis Detection Rates in Postmenopausal Women," Int. J. Endocrinol., **2013**.
[50] Kanis, J. A., McCloskey, E. V., Johansson, H., Cooper, C., Rizzoli, R., and Reginster, J. Y., 2013, "European Guidance for the Diagnosis and Management of Osteoporosis in Postmenopausal Women," Osteoporos. Int., **24**(1), pp. 23–57.
[51] Cummings, S. R., Bates, D., and Black, D. M., 2002, "Clinical Use of Bone Densitometry: Scientific Review," Jama, **288**(15), pp. 1889–1897.
[52] Kanis, J. A., Oden, A., Johnell, O., Johansson, H., De Laet, C., Brown, J., Burckhardt, P., Cooper, C., Christiansen, C., Cummings, S., Eisman, J. A., Fujiwara, S., Glüer, C., Goltzman, D., Hans, D., Krieg, M. A., La Croix, A., McCloskey, E., Mellstrom, D., Melton, L. J., Pols, H., Reeve, J., Sanders, K., Schott, A. M., Silman, A., Torgerson, D., Van Staa, T., Watts, N. B., and Yoshimura, N., 2007, "The Use of Clinical Risk Factors Enhances the Performance of BMD in the Prediction of Hip and Osteoporotic Fractures in Men and Women," Osteoporos. Int., **18**(8), pp. 1033–1046.
[53] Premaor, M. O., Pilbrow, L., Tonkin, C., Adams, M., Parker, R. A., and Compston, J., 2009, "Low Rates of Treatment in Postmenopausal Women with a History of Low Trauma Fractures: Results of Audit in a Fracture Liaison Service," Qjm, **103**(1), pp. 33–40.
[54] McLellan, A. R., Gallacher, S. J., Fraser, M., and McQuillian, C., 2003, "The Fracture Liaison Service: Success of a Program for the Evaluation and Management of Patients with Osteoporotic Fracture," Osteoporos. Int., **14**(12), pp. 1028–1034.
[55] Cummings, S. R., and Melton, L. J., 2002, "Osteoporosis I: Epidemiology and Outcomes of Osteoporotic Fractures," Lancet, **359**(9319), pp. 1761–1767.
[56] Eriksen, E. F., 2010, "Cellular Mechanisms of Bone Remodeling," Rev. Endocr. Metab. Disord., **11**(4), pp. 219–227.
[57] Hansen, M. A., Overgaard, K., and Christiansen, C., 1995, "Spontaneous Postmenopausal Bone Loss in Different Skeletal Areas—followed up for 15 Years," J. Bone Miner. Res., **10**(2), pp. 205–210.
[58] Arlot, M. E., Sornay-Rendu, E., Garnero, P., Vey-Marty, B., and Delmas, P. D., 1997, "Apparent Pre- and Postmenopausal Bone Loss Evaluated by DXA at Different Skeletal Sites in Women: The OFELY Cohort," J. Bone Miner. Res., **12**(4), pp. 683–690.
[59] Kutzner, I., Heinlein, B., Graichen, F., Bender, A., Rohlmann, A., Halder, A., Beier, A., and Bergmann, G., 2010, "Loading of the Knee Joint during Activities of Daily Living Measured in Vivo in Five Subjects," J. Biomech., **43**(11), pp. 2164–2173.
[60] Heller, M. O., Bergmann, G., Deuretzbacher, G., Dürselen, L., Pohl, M., Claes, L., Haas, N. P., and Duda, G. N., 2001, "Musculo-Skeletal Loading Conditions at the Hip during Walking and Stair Climbing," J. Biomech., **34**(7), pp. 883–893.

[61] Rohlmann, A., Pohl, D., Bender, A., Graichen, F., Dymke, J., Schmidt, H., and Bergmann, G., 2014, "Activities of Everyday Life with High Spinal Loads," PLoS One, **9**(5), pp. 1–10.
[62] Kutzner, I., Heinlein, B., Graichen, F., Bender, A., Rohlmann, A., Halder, A., Beier, A., and Bergmann, G., 2010, "Loading of the Knee Joint during Activities of Daily Living Measured in Vivo in Five Subjects," J. Biomech., **43**(11), pp. 2164–2173.

Tables

Table 1: Descriptive characteristics of the control and fracture groups and details of fracture sites incurred prior to imaging*

Variable	Control group (N=23)	Fracture group (N=23)	P value
Age (yrs)	64.8±6.8	64.4±8.3	0.593
Height (cm)	162.3±5.5	159.2±8.9	0.096
Weight (kg)	68.1±14.7	66.2±10.8	0.983
BMI (kg/cm^2)	25.9±5.6	26.2±4.3	0.593
L_{tibia} (cm)	35.5±1.6	33.0±3.5	0.096
Fracture site[1]			
Contralateral tibia or fibula	0	5	
Ankle or foot	0	1	
Femur	0	1	
Humerus	0	3	
Radius	0	15	

L_{tibia}, tibia length; BMI, body mass index.
*Significant differences between the groups were assessed by a two-sample Kolmogorov-Smirnov test
[1] Note: one fracture group patient sustained a fracture at both the radius and contralateral tibia, whilst another sustained both radial and humeral fracture.

Table 2: FE model variables computed for different cubic element sizes at the 4% and 66% sites of a representative control subject. Diff. indicates the percentage difference of each stiffness from the value computed with a cubic element size of 0.1 mm.

Site	Cubic element size (mm)	k_{comp}		k_{shear}		$k_{torsion}$		k_{bend}	
		Value (kN/mm)	Diff. (%)	Value (kN/mm)	Diff. (%)	Value (Nm/deg)	Diff. (%)	Value (Nm/deg)	Diff. (%)
4% site	1	1242.4	0.0	11.3	-96.7	1213.0	-1.5	67.8	-96.2
	0.4*	1256.7	1.1	345.1	1.4	1244.8	1.1	1824.4	1.4
	0.2	1245.9	0.2	341.8	0.4	1234.6	0.3	1805.5	0.3
	0.1	1242.9	N/A	340.4	N/A	1231.4	N/A	1799.8	N/A
66% site	1	3814.9	0.6	1115.2	2.4	2940.3	0.0	2704.7	0.4
	0.4*	3818.7	0.7	1100.6	1.1	2957.0	0.5	2719.8	0.9
	0.2	3798.0	0.2	1092.0	0.3	2945.7	0.2	2701.7	0.2
	0.1	3791.5	N/A	1088.9	N/A	2941.0	N/A	2695.2	N/A

k_{comp}, compressive stiffness; k_{shear}, shear stiffness; $k_{torsion}$, torsional stiffness; k_{bend}, bending stiffness.
*Original element size of FE models.

Table 3: Calculation of compressive, shear, torsional and bending stiffness at the 4% and 66% sites for a representative participant of the control group.

	4% site		66% site	
Load case	Reaction force or moment	Stiffness	Reaction force or moment	Stiffness
Compression	12514.5 N	1251.5 kN/mm	38129.1 N	3812.9 kN/mm
Shear	3430.2 N	343.0 kN/mm	10984.9 N	1098.5 kN/mm
Torsion	7.1 Nm	1238.0 Nm/deg	16.9 Nm	2952.5 Nm/deg
Bending	10.4 Nm	1816.9 Nm/deg	15.5 Nm	2709.5 Nm/deg

Table 4: DXA, pQCT, structural and FE model properties derived for the control and fracture groups[a]. Values are specified where applicable for the 4% and 66% sites of the tibia.

	Variable	Control Group (N=23)	Fracture Group (N=23)	p-value
DXA properties	aBMD lumbar spine (mg/cm^2)	964.8±201.9	874.8±139.8	0.096
	aBMD femoral neck (mg/cm^2)	732.9±119.7	679.1±94.6	0.593
	aBMD total hip (mg/cm^2)	907.2±167.1	788.3±116.2	0.593

		4% site			66% site		
	Variable	Control Group (N=23)	Fracture Group (N=23)	p-value	Control Group (N=23)	Fracture Group (N=23)	p-value
pQCT properties	a_{tot} (mm^2)	1132.8±184.3	1181.3±162.0	0.360	571.9±62.4	552.3±96.9	0.593
	ρ_{tot} (mg/cm^3)	279.8±55.2	222.7±38.9	0.002	622.6±100.1	617.2±110.9	0.842
	SSI_x (mm^2)	405.5±216.8	317.2±184.9	0.195	1527.9±212.3	1377.3±289.5	0.195
	SSI_y (mm^2)	225.9±188.3	143.5±152.8	0.360	879.7±165.9	794.9±175.9	0.195
	SSI_{pol} (mm^2)	547.9±360.0	388.8±296.0	0.195	2128.2±330.2	1917.0±407.5	0.360
Structural properties	EA (10^6 N)	1.8±0.5	1.3±0.4	0.002	5.5±1.0	5.1±1.0	0.195
	GJ ($N\bullet m^2$)	152.9±38.6	118.2±31.9	<0.001	298.9±60.4	265.7±71.9	0.360
	EI_x ($N\bullet m^2$)	221.5±57.5	170.9±44.1	<0.001	547.3±102.7	483.6±137.1	0.360
	EI_y ($N\bullet m^2$)	175.5±44.8	136.1±39.5	0.006	228.3±64.6	205.7±58.8	0.593
Finite element model properties	k_{comp} (kN/mm)	1148.8±325.1	821.0±233.4	<0.001	3361.7±671.8	3125.6±668.0	0.195
	k_{shear} (kN/mm)	318.2±92.6	221.8±64.9	<0.001	963.8±198.4	896.4±197.3	0.195
	$k_{torsion}$ (Nm/deg)	1279.9±328.8	977.5±273.0	<0.001	2532.1±517.1	2240.4±611.5	0.360
	k_{bend} (Nm/deg)	1871.4±484.7	1430.2±411.3	<0.001	2386.1±689.6	2144.4±621.5	0.593

aBMD, areal bone mineral density; a_{tot}, total area; ρ_{tot}, total density; SSI_x and SSI_y stress-strain indices about the x- and y-axes, respectively; SSI_{pol}, torsional stress-strain index, EA, axial rigidity; EI_x and EI_y bending rigidity about the x- and y-axes, respectively; GJ, torsional rigidity; k_{comp}, compressive stiffness; k_{shear}, shear stiffness; $k_{torsion}$, torsional stiffness; k_{bend}, bending stiffness.

[a] Significant differences between the groups were assessed by a two-sample Kolmogorov-Smirnov test.

Table 5: Variance inflation factor (VIF) of DXA, pQCT, structural and FE model properties derived for the control and fracture groups. Values are specified where applicable for the 4% and 66% imaging sites of the tibia.

		VIF	
Modality	Variable	Control Group (N=23)	Fracture Group (N=23)
DXA properties	Age	1.4	1.2
	Height	1.6	1.4
	Weight	2.3	1.5
	aBMD lumbar spine	4.1	1.4
	aBMD femoral neck	11.0	4.0
	aBMD total hip	16.7	3.7

		VIF, 4% site		VIF, 66% site	
Modality	Variable	Control Group (N=23)	Fracture Group (N=23)	Control Group (N=23)	Fracture Group (N=23)
pQCT properties	Age	1.9	1.6	1.6	1.4
	Height	2.2	2.1	1.9	1.9
	Weight	2.0	2.3	3.0	1.5
	a_{tot}	5.2	6.9	55.3	44.9
	ρ_{tot}	5.1	6.4	56.7	21.4
	SSI_x	31.8	103.1	18.1	37.8
	SSI_y	83.4	281.5	38.7	20.6
	SSI_{pol}	143.4	671.3	101.8	77.2
Structural properties	Age	1.3	1.4	1.2	1.2
	Height	1.8	1.7	1.6	2.1
	Weight	2.3	1.5	1.7	1.2
	EA	5.6	12.9	2.9	2.7
	GJ	15.1	30.1	8.5	8.2
	EI_x	9.4	32.3	2.3	2.8
	EI_y	13.1	18.3	5.8	5.9

Finite element model properties	Age	2.9	1.4	1.3	1.3
	Height	2.3	1.7	1.6	2.3
	Weight	3.3	1.4	2.1	1.6
	k_{comp}	2298.6	441.6	5398.2	3753.6
	k_{shear}	2301.5	419.6	5311.0	3548.2
	$k_{torsion}$	39.4	80.1	21.3	34.3
	k_{bend}	35.7	56.3	21.5	18.5

aBMD, areal bone mineral density; a_{tot}, total area; ρ_{tot}, total density; SSI_x and SSI_y stress-strain indices about the x- and y-axes, respectively; SSI_{pol}, torsional stress-strain index, EA, axial rigidity; EI_x and EI_y bending rigidity about the x- and y-axes, respectively; GJ, torsional rigidity; k_{comp}, compressive stiffness; k_{shear}, shear stiffness; $k_{torsion}$, torsional stiffness; k_{bend}, bending stiffness.

Table 6: Odds ratio, sensitivity, specificity and area under curve (AUC) of receiver operative characteristic curve derived for DXA, pQCT, structural and FE-model properties[a,b]. Values are specified where applicable for the 4% and 66% imaging sites of the tibia.

Imaging modality	Variable	Odds ratio (95% CI)	Sensitivity (%)	Specificity (%)	AUC (95% CI)
DXA properties	aBMD lumbar spine	**1.77 (0.84-3.72)**	**43.48**	**91.30**	**0.64 (0.48-0.81)**
	aBMD femoral neck	1.65 (0.78-3.48)	-	-	-
	aBMD total hip	**2.98 (1.24-7.13)***	**82.61**	**56.52**	**0.71 (0.56-0.86)**

		4%				66%			
Imaging modality	Variable	Odds ratio (95% CI)	Sensitivity (%)	Specificity (%)	AUC (95% CI)	Odds ratio	Sensitivity (%)	Specificity (%)	AUC (95% CI)
pQCT properties	a_{tot}	1.97 (0.88-4.42)	-	-	-	1.07 (0.54-2.15)	-	-	-
	ρ_{tot}	**12.86 (2.51-65.76)****	**73.91**	**78.26**	**0.80 (0.67-0.93)**	1.05 (0.56-1.97)	-	-	-
	SSI_x	1.88 (0.82-4.29)	-	-	-	**2.02 (0.80-5.08)**	**82.61**	**47.83**	**0.65 (0.49-0.81)**
	SSI_y	1.86 (0.84-4.13)	-	-	-	1.63 (0.72-3.69)	-	-	-
	SSI_{pol}	1.93 (0.85-4.37)	-	-	-	1.89 (0.79-4.51)	-	-	-
Structural properties	EA	**10.51 (2.07-53.44)****	**73.91**	**78.26**	**0.80 (0.67-0.93)**	**1.34 (0.62-2.91)**	**39.13**	**91.30**	**0.61 (0.44-0.77)**
	GJ	6.70 (1.62-27.74)*	-	-	-	**1.64 (0.68-3.92)**	**47.83**	**78.26**	**0.63 (0.46-0.79)**
	EI_x	6.44 (1.61-25.81)*	-	-	-	**1.72 (0.70-4.21)**	**65.22**	**60.87**	**0.63 (0.47-0.80)**
	EI_y	5.78 (1.55-21.57)**				1.31 (0.62-2.77)	-	-	-

Finite element model properties	k_{comp}	13.46 (2.32-77.97)**	-	-	-	1.33 (0.61-2.87)	-	-	-
	k_{shear}	**16.09 (2.52-102.56)****	**78.26**	**82.61**	**0.81 (0.69-0.94)**	1.31 (0.61-2.81)	-	-	-
	$k_{torsion}$	7.34 (1.69-31.88)**	-	-	-	**1.69 (0.7-4.06)**	**47.83**	**78.26**	**0.63 (0.47-0.79)**
	k_{bend}	6.80 (1.68-27.52)**	-	-	-	1.32 (0.62-2.80)	-	-	-

a_{tot}, total area; ρ_{tot}, total density; SSI_x and SSI_y, stress-strain indices about the x- and y-axes, respectively; SSI_{pol}, torsional stress-strain index, EA, axial rigidity; EI_x and EI_y, bending rigidity about the x- and y-axes, respectively; k_{shear}, shear stiffness; $k_{torsion}$, torsional stiffness. **Bold text,** data for variables included in the classification analysis, based on their collinearity assessment and greater odds ratio.

[a] Adjusted for age, height and weight.

[b] Significance of odds ratio tested with respect to null hypothesis (i.e., classification based on chance).

* $p<0.05$

** $p<0.01$

Figure captions

Fig. 1. Diagram of pQCT imaging sites and the mapping of apparent density (ρ_{app}) and Young's modulus. **A** Location of 4% and 66% sites on tibia. L_{tibia}, length of tibia estimated as distance from medial malleolus to inferior apex of patella. Representative pQCT images obtained at the 66% and 4% sites are provided. **B** Contour plot of ρ_{app} at 66% and 4% sites. **C** Contour plot of Young's modulus at 66% and 4% sites. The origin was aligned with the density weighted centroid of each cross-section and the x- and y-axes were aligned with the minimum and maximum neutral axes, respectively.

Fig. 2. Diagram of FE model mesh of a representative specimen at the 66% site. Contours corresponding to different Young's moduli are included in each picture. **A** FE model mesh generated by a 2 mm extrusion of the pQCT image. **B** Inset to part A showing the rectangular elements. **C** FE model mesh after re-slicing axially. **D** Inset to part C showing the 0.4 mm cubic elements. The origin of the models was set as the density-weighted centroid (Eq. 9), the x- and y-axes were aligned with the minimum and maximum neutral axes, respectively, and the z-axis was normal to the cross-section.

Fig. 3. Diagram of the load cases applied to each cross-section. The FE mesh corresponds to a representative specimen at the 66% site and the contours representing different Young's moduli are included in each picture. **A** Compression load case, corresponding to a 0.01 mm displacement. *Red arrows* applied displacement of 0.01 mm in the negative z direction. *Red triangles* fixed boundary condition applied to surface. **B** Shear load case. Red arrows applied a displacement of 0.01 mm in either the positive x direction or y direction. **C** Torsion load case. *Red arrow* applied

rotation of 0.0001 radians about the z-axis. **D** Bending load case. *Red arrow* applied rotation of 0.0001 radians about either the x- or y-axis.

Fig. 4. FE model meshes corresponding to a different cubic element sizes that were used in the verification analysis. The FE models describe a 4% site (top row) and 66% site (bottom row) of a representative participant of the control group. FE models corresponded to cubic element sizes of 1.0, 0.4, 0.2 and 0.1 mm, (**A**, **B**, **C** and **D**, respectively). Close-up views of the FE model mesh with a 0.1 mm cubic element size are shown for the 4% and 66% sites (**E** and **F**, respectively).

Fig. 5: Principal stresses predicted for compression, shear, torsion and bending predicted by the FE model at the 4% and 66% sites of a representative control participant. **A** Maximum principal stress predicted for each load case at the 4% site. **B** Minimum principal stress predicted for each load case at the 4% site. **C** Maximum principal stress predicted for each load case at the 66% site. **D** Minimum principal stress predicted for each load case at the 66% site. Due to significantly different stresses for each load case, the contours are expressed relative to the maximum and minimum stresses.

Fig. 6. Box and whisker plot of key pQCT, FE model structural and DXA properties compared between the controls and fracture group. Variables include DXA: aBMD total hip, areal bone mineral density measured for the total hip by DXA; ρ_{tot}, total density obtained by pQCT at the 4% site; SSIx, stress-strain index about the x-axis at the 4% site; SSIpol, polar stress-strain index at the 4% site; k_{shear}, shear stiffness at the 4% site; EA, axial rigidity at the 4% site. The red line represents the median, the edges of the box are the 25th and 75th percentiles, and the whiskers extend to the maximum and minimum of the data. Red crosses indicate outliers in the data. * $p< 0.05$, ** $p<0.001$.

Fig. 1

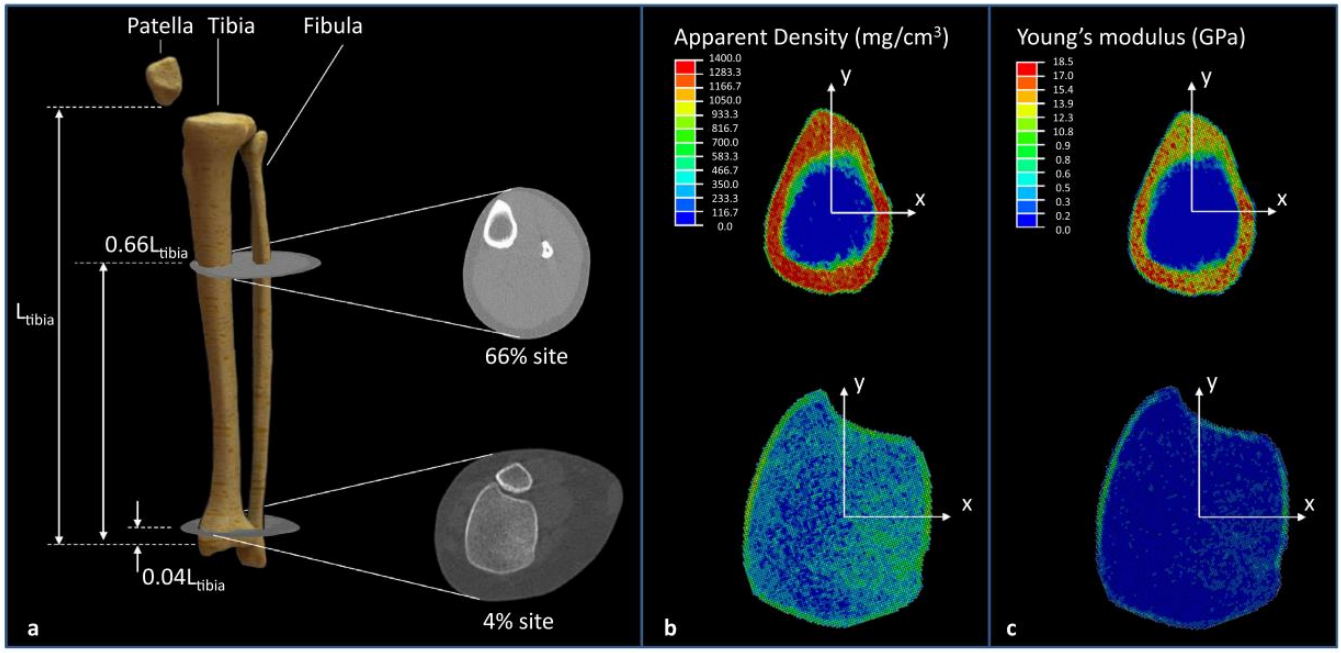
Patella
Tibia
Fibula
0.66L tibia
L tibia
66% site
0.04L tibia
4% site
a
Apparent Density (mg/cm³)
1400.0
1283.3
1166.7
1050.0
933.3
816.7
700.0
583.3
466.7
350.0
233.3
116.7
0.0
y
x
b
Young's modulus (GPa)
18.5
17.0
15.4
13.9
12.3
10.8
0.9
0.8
0.6
0.5
0.3
0.2
0.0
c

Fig. 2

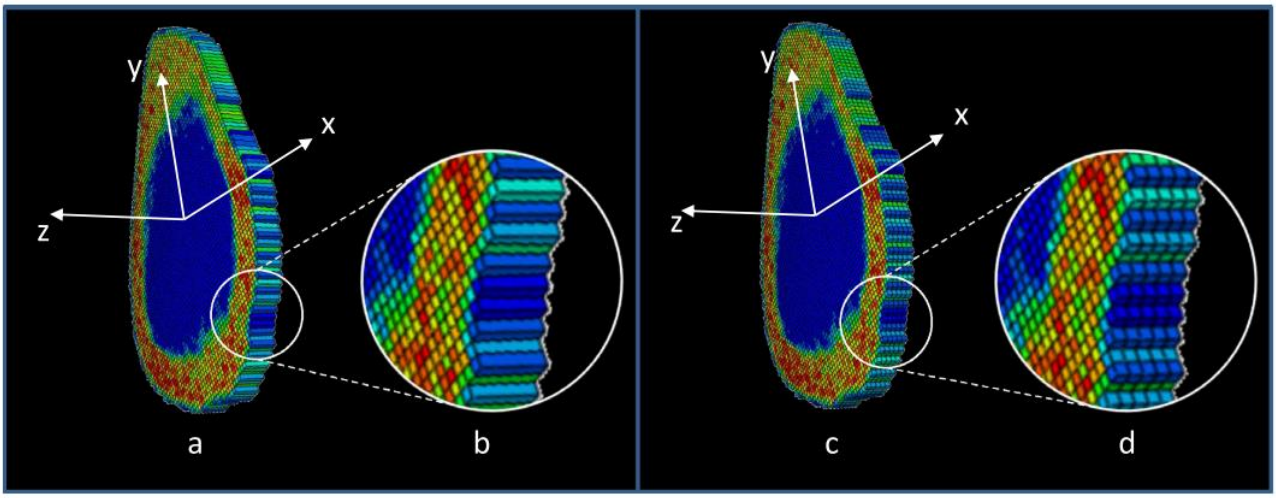

Fig. 3

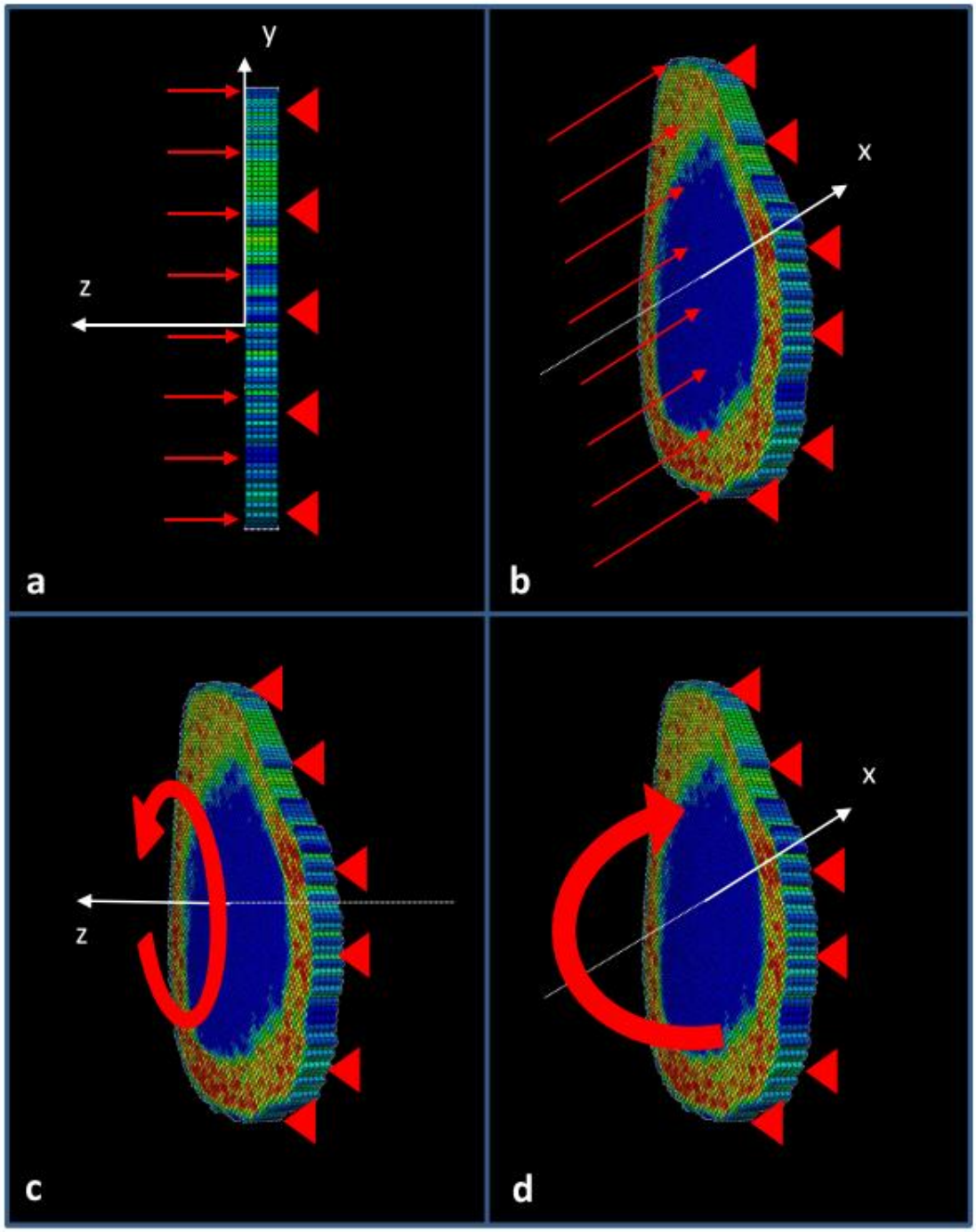

Fig. 4

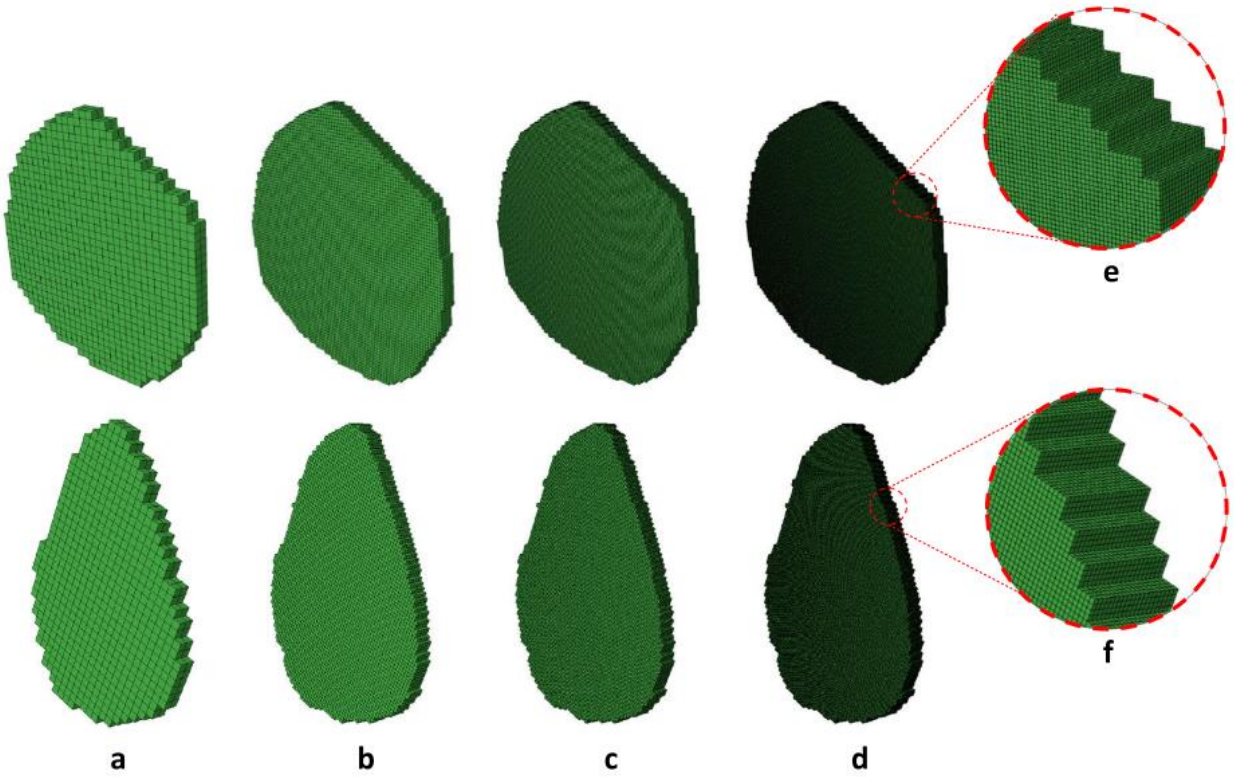

Fig. 5

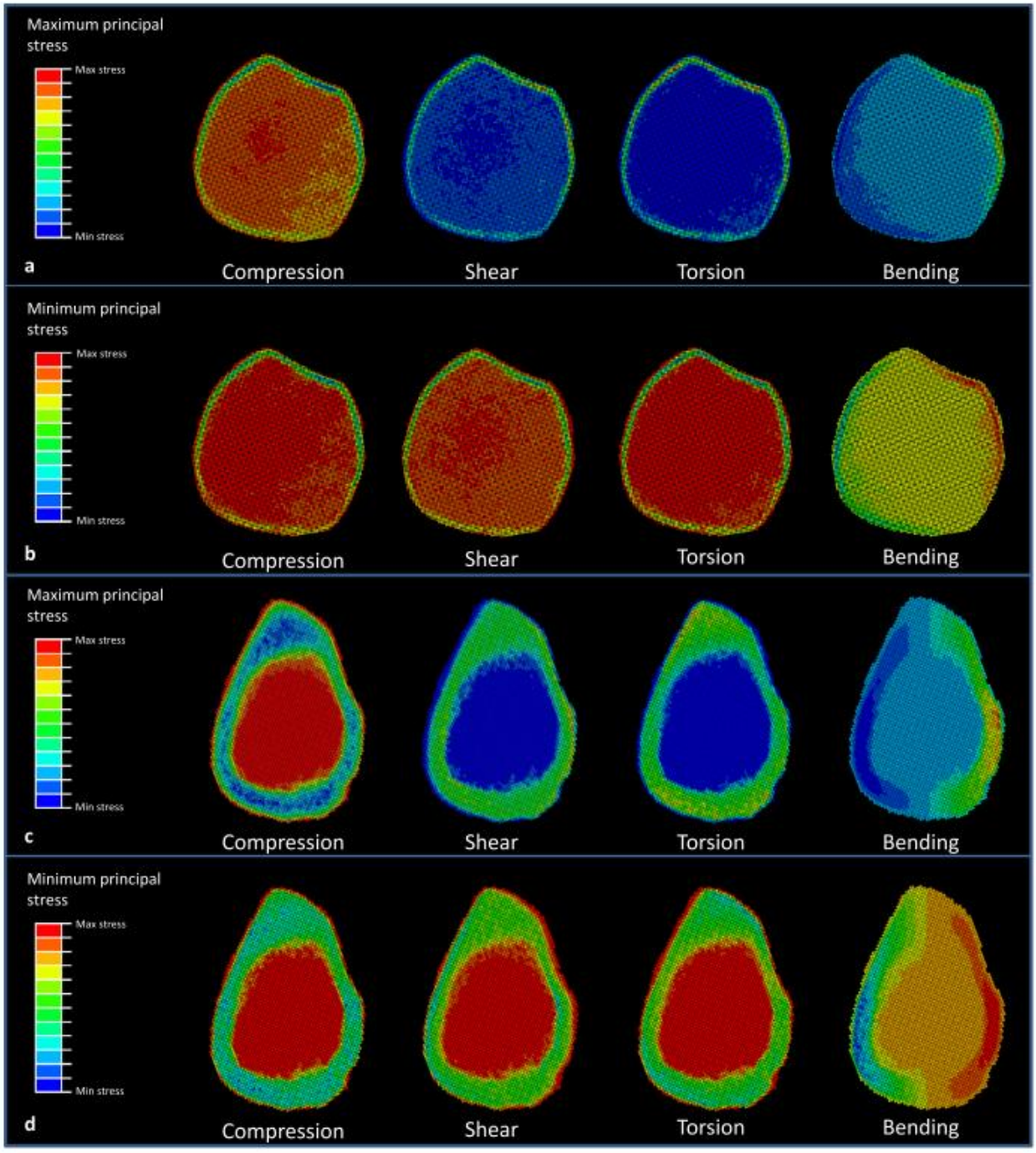
Maximum principal stress
Max stress
Min stress
a
Compression
Shear
Torsion
Bending
Minimum principal stress
Max stress
Min stress
b
Compression
Shear
Torsion
Bending
Maximum principal stress
Max stress
Min stress
c
Compression
Shear
Torsion
Bending
Minimum principal stress
Max stress
Min stress
d
Compression
Shear
Torsion
Bending

Fig. 6

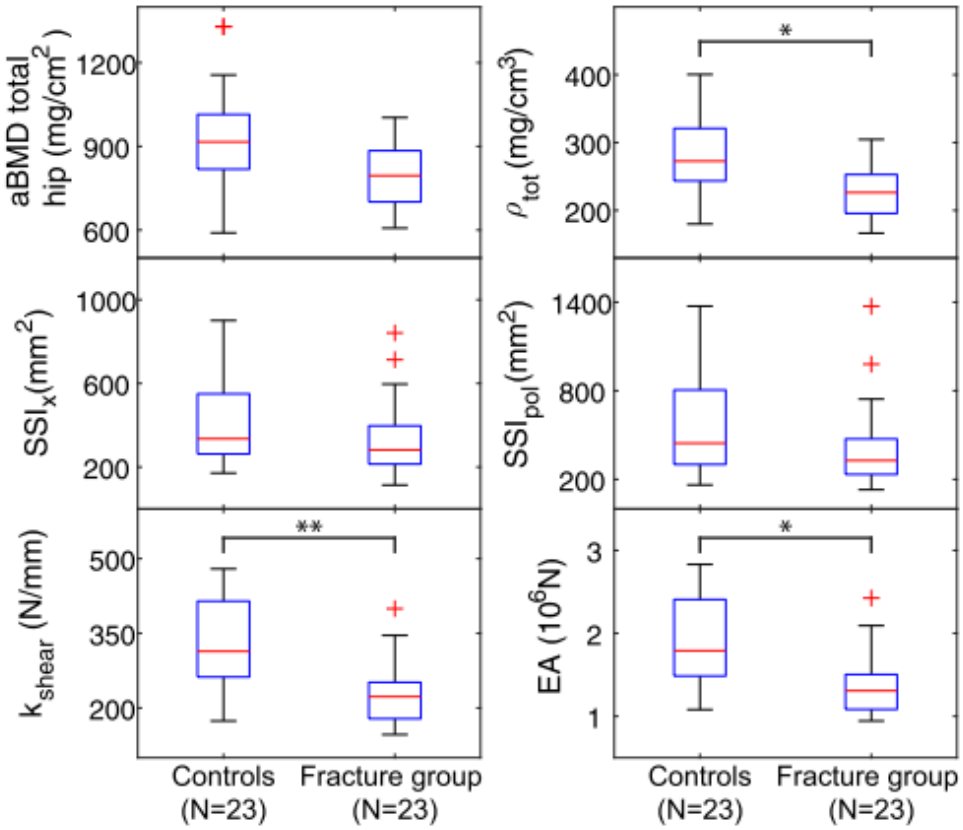
aBMD total hip (mg/cm²)
1200
900
600
ρtot (mg/cm³)
400
300
200
*
SSIx(mm²)
1000
600
200
SSIpol(mm²)
1400
800
200
kshear (N/mm)
500
350
200
**
EA (10⁶N)
3
2
1
*
Controls (N=23)
Fracture group (N=23)
Controls (N=23)
Fracture group (N=23)